JOURNAL OF COMPUTATIONAL PHYSICS 119, 195–205 (1995)

Numerical Investigation of an Analytic Solution of a Multi-dimensional Lippman–Schwinger Seismic Inverse Problem

DAVID B. GRAY AND GEORGE A. MCMECHAN

The Center for Lithospheric Studies, The University of Texas at Dallas, P.O. Box 830688, Richardson, Texas 75083-0688

Received April 13, 1992; revised January 19, 1995

The analytic solution of the Lippman–Schwinger seismic inverse problem in three spatial dimensions, assuming a point source and a constant-density earth model, is valid in the spatial zero frequency limit. It is expressed as a two-dimensional inverse Fourier transform followed by an inverse Laplace transform. For the case of laterally homogeneous velocity, the analytic solution is correct when applied to a forward solution of the wave equation for a single-interface velocity model. Error surfaces of the non-linear, iterative, least-squares inversions corresponding to multiple, constant-velocity, horizontal layers have an absolute minimum at or near the location of the solution parameters for zero and low frequencies. The error surface for a scattered wavefield dataset generated by 3D finite-difference modeling combined with *a priori* constraints, produces nearly correct solutions for a range of low frequencies. Thus, this approach has potential for applicability to field data.

1. INTRODUCTION

The wave-equation has been for some time the basis for modern inversion techniques to estimate the material properties of the earth's subsurface from observations of the scattered wavefield. Even so, approaches have varied widely. Pre-stack migration may be considered a simpler form of wave-equation inversion [2, 15, 21]. Several authors have studied the inversion problem for velocity and the location and character of seismic reflectors [7]. Seismic inversion is closely related to migration, but the solutions resulting from inversion quantitatively account for reflections and yield spatial changes in parameters that cause the reflections (e.g., density and bulk modulus).

Inversion for velocity can also be expressed as a time-domain form of Born inversion [22]. A classic solution to the scattering problem, Born inversion utilizes perturbation and approximation techniques. It has recently undergone serious investigation [12] and comparison with migration techniques [19].

Another inversion approach assumes a parameterized model and attempts to estimate the model parameters from the scattered wavefield, creating a very large non-linear, iterative problem [20]. Formulations for inversion have also been done in the slowness-time intercept domain [5, 11]. An extensive review and summary of wave-equation inversion techniques with a large collection of references is given in [22].

This study uses an inversion method based upon the Lippman–Schwinger form of the wave equation. One popular solution of this equation uses the Born approximation. The Born approximation linearizes the wave equation by ignoring transmissions and secondary reflections. It requires an *a priori* estimate of the medium parameters in the constant or slowly varying background function. The Born approximation solves for a perturbation of the background; the scattered wavefield is attributed to this perturbation. Since the background is defined *a priori*, solving for the perturbation amounts to solving the entire problem. A solution that develops the Lippman–Schwinger equation and the Born approximation for precritical offset data is given in [6]. WKBJ Green's operators are used to solve for density and bulk modulus, assuming a smoothly varying background. Another solution using the Born approximation, with constant background for velocity and density, shows that multiple datasets are required to solve for multiple parameters [18].

Many difficulties with the Born approximation have been discovered and analyzed. Parameter variations can cause artifacts in the perturbation solutions of other parameters [24]. Because the Born approximation ignores multiples, the quality of the solution degrades with depth [24]. Also, Born solutions are sensitive to the choice of the background functions [23].

The theoretical framework for the present paper is an analytic solution of the Lippman–Schwinger equation [16] solved in the low-frequency limit for a point source in a three-dimensional, constant-density medium. This solution is an alternative to the Born approximation; it makes no assumptions about the background or the perturbation. It fully incorporates pre- and post-critically reflected data and ignores none of the scattered wavefield in the zero frequency limit. In this limit, it incorporates all non-linear wavefield phenomena such as multiples and transmission effects, potentially avoiding the shortcomings of Born inversion. Being a 3D formulation enhances its importance as 3D surveys become increasingly common.

As a first step, this investigation assumes a constant-density

0021-9991/95 $6.00

medium. This constraint can be relaxed; two contrasting solutions for density and bulk-modulus perturbations with respect to a constant background and inversion solutions in 1D and 2D are presented in [17, 13], respectively.

A review of the theoretical basis for analytical and numerical experimentation is presented in the next section. The solution is shown to reduce to an inverse Laplace operation when the velocity of the earth model is laterally homogeneous. An analytical expression for the reflected wavefield from a single velocity interface is then used as a test; when substituted into the inverse solution, the correct expression for the velocity is found.

When the earth model is assumed to consist of horizontal, constant-velocity layers, the inverse problem can easily be cast into a non-linear, iterative, least-squares problem. The model parameters to be determined are the interface depths and the layer velocities. A two-layer case is then investigated using a numerical dataset computed from the analytical expression. The solution to the non-linear problem gives the correct depth and velocity for very low frequencies but yields less accurate solutions as frequency increases.

Finally, an independent dataset is generated with a 3D finite-difference program and used as input to the non-linear problem. For a range of low frequencies, the least-squares solution again yields acceptable solutions.

We attempt to show that this inversion technique is a potentially viable solution to real seismic inverse problems. Although very low frequencies are required, they are not below the range of modern recording equipment. The question of whether solutions in the low-frequency limit are meaningful is answered here in the positive by the results presented. An explanation of the intuitive meaning of zero-limit solutions is a topic of ongoing discussion and is not attempted here.

2. THEORY

This section contains the theoretical basis of our inversion. The goal is to find the velocity distribution that produces the reflected pressure waves measured at the surface of the earth when the earth is excited with a seismic source. The problems considered are a point source in a 3D medium and a plane wave source in a 1D medium. Subsequent investigations are limited to the 3D formulation.

2.1. *Three-Dimensional Inverse Theory*

Solution of the scalar wave equation, the inhomogeneous Helmholtz equation for a scalar wavefield $u = u(\omega, \mathbf{x}, \mathbf{y})$, for a point source function at location $\mathbf{x} = (x_1, x_2, x_3)$, assuming constant density through a medium with velocity c is [16]

$$\nabla^2 u + \frac{\omega^2}{c^2(\mathbf{x})} u = -\delta(\mathbf{x} - \mathbf{y}), \tag{1}$$

where $\mathbf{y} = (y_1, y_2, y_3)$ is the receiver location and ω is the angular frequency. Given a velocity distribution of the form

$$c^{-2}(\mathbf{x}) = c_0^{-2}(1 + v(\mathbf{x})), \tag{2}$$

where c_0 is a constant background velocity and $v(\mathbf{x})$ the velocity perturbation from c_0 at location $\mathbf{x}$, then, after transformation and rearrangement of Eq. (1), the Lippman–Schwinger equation [6] with scattering potential v is

$$u = g + k^2 \int_{-\infty}^{+\infty} \mathbf{dz}\, g(\mathbf{x}, \mathbf{z}) v(\mathbf{z}) u(\mathbf{z}, \mathbf{y}), \tag{3}$$

where g is the three-dimensional Green's function and $\mathbf{z} = (z_1, z_2, z_3)$ is a spatial vector. The Born approximation results from assuming that, to first order, u can be approximated by g.

After subtracting the direct arrival from the scattered field and taking the 2D Fourier transform of the zero frequency limit of the ratio of the reflected data and the square of the wavenumber, $F(\mathbf{p}', q/2)$ can be obtained from $u(\omega, \mathbf{x}, \mathbf{y})$ (Appendix A). Then the solution for the perturbation is (when it has compact support; i.e., it is defined within a closed region) [16]

$$v(\mathbf{z}) = \frac{1}{2\pi i} \int_{-\infty}^{+\infty} \int_{-\infty}^{+\infty} \mathbf{dp}' \int_{c-i\infty}^{c+i\infty} dq\, F(\mathbf{p}', q/2) \exp(q\mathbf{z} - i(\mathbf{p}' \cdot \mathbf{z}')), \tag{4}$$

where $\mathbf{p}' = (p_1, p_2)$ are Fourier transform variables, q is a Laplace transform variable, $\mathbf{z} = -z_3$, $c > 0$ is a constant, and $\mathbf{z}' = (z_1, z_2)$. The velocity perturbation $v(\mathbf{z})$ is given as a 2D inverse spatial Fourier transform followed by an inverse 1D spatial Laplace transform.

2.2. *Lateral Velocity Homogeneity*

In this section the problem is simplified to a 1D space. The procedure will be very similar to that described above, except the velocity is assumed to be laterally homogeneous. The 1D scalar wave equation replaces the corresponding 3D equation of the previous section. The solution is found to be simply an inverse spatial Laplace transform.

Let the velocity be laterally homogeneous, so that

$$v(x_1, x_2, x_3) = v(x_3). \tag{5}$$

Now, consider the 1D, scalar, constant-density, Helmholtz equation

$$\{\nabla^2 + k^2[1 + v(x_3)]\} u(\mathbf{x}) = -\delta(\mathbf{x}). \tag{6}$$

Since the velocity is independent of x_1 and x_2, the two-dimensional Fourier transform of Eq. (6) is

$$\left[\frac{d^2}{dx_3^2} - \lambda^2 + k^2 + k^2 v\right] U(\boldsymbol{\lambda}, x_3) = -\delta(x_3), \tag{7}$$

where $\boldsymbol{\lambda}$ is the two-dimensional transform vector. The corresponding Lippman–Schwinger equation is

$$U(\boldsymbol{\lambda}, x_3) = g'(x_3) + k^2 \int_{-\infty}^{+\infty} dz_3 g'(x_3 - z_3) v(z_3) U, \tag{8}$$

where the 1D Green's function is of the form

$$g'(x_3) = \frac{\exp(-i(k^2 - \boldsymbol{\lambda}^2)^{1/2} |x_3|)}{2i(k^2 - \lambda^2)^{1/2}}, \quad \lambda^2 > k^2. \tag{9}$$

Taking the low frequency limit gives

$$f(\boldsymbol{\lambda}, x_3) = \lim_{k \to 0} \frac{U - g'}{k^2} = \lim_{k \to 0} \int_{-\infty}^{+\infty} dz_3 g(x_3 - z_3) v(z_3) g(x_3), \tag{10}$$

where

$$g(x_3) = \frac{1}{2|\lambda|} \exp(-|\lambda| |x_3|). \tag{11}$$

If f is measured at the surface so that $x_3 = 0$, then Eq. (10) becomes

$$4\lambda^2 f(\boldsymbol{\lambda}) = \int_{-\infty}^{+\infty} dz_3 v(z_3) \exp(-2|\lambda| |z_3|). \tag{12}$$

By making the changes of variables, $2|\lambda| = q$ for $\lambda > 0$, and $u = -z_3$, and assuming that, for $z_3 > 0$, $v(x_3) = 0$, a simpler expression

$$q^2 F(q/2) = \int_0^{\infty} du\, v(-u) \exp(qu) \tag{13}$$

is obtained. Let $G(q) = q^2 F(q/2)$. The solution for $v(z_3)$ can then be written as an inverse Laplace transform,

$$v(u) = 2L^{-1}(G(q)), \quad u = -z_3. \tag{14}$$

3. ANALYTICAL EXAMPLE

The theoretical solution, Eq. (14), can be tested analytically. An analytical forward solution to the scalar wave-equation from [9] for two liquid half-spaces is used to generate "data" for the inverse problem in [16]. The solution is expressed in the Fourier–Bessel transform domain and can be used to find the transform of the observed function F in Eq. (4). The problem here is to find the velocity perturbation, $v(\mathbf{z})$, given the analytical forward wavefield solution of the wave equation, F.

The solution simplifies to

$$q^2 F(q/2) = 4 \int_0^{\infty} du \exp(-qu) v(-u), \tag{15}$$

where q is the Laplace transform variable in Eq. (4) and when cylindrical symmetry is assumed (Appendix A). Indeed, this is quite similar to Eq. (13) which is the analogous 1D formulation.

The low frequency limit of the analytical solution (Appendix B) from [9] is

$$q^2 F(q/2) = 4c_0^2(\alpha_2^{-2} - \alpha_1^{-2}) \frac{\exp(-qh)}{q}, \tag{16}$$

where h is the depth to the interface of the half-spaces, α_1 is the velocity of the upper half-space, and α_2 is the velocity of the lower half-space. This expression provides the "data" F for the analytical test of the inversion. Substituting Eq. (15) into (16) yields

$$c_0^2(\alpha_2^{-2} - \alpha_1^{-2}) \frac{\exp(-qh)}{q} = \int_0^{\infty} du \exp(-qu) v(-u). \tag{17}$$

Using the Laplace transform pair [1],

$$L^{-1}\left(\frac{\exp(-ks)}{s}\right) = S_k(t) = \begin{cases} 0, & 0 < t < k, \\ 1, & t > k, \end{cases} \tag{18}$$

the solution for v, if $c_0 = \alpha_1$, is

$$v(-u) = \begin{cases} 0 & \text{for } 0 < u < h \\ \left(\dfrac{\alpha_1^2}{\alpha_2^2} - 1\right) & \text{for } u > h \end{cases} \tag{19}$$

which is exactly the original perturbation. Thus the inversion [16] exactly solves the inverse of the forward problem given by [9].

4. NUMERICAL EXAMPLE

In this section, the laterally homogeneous velocity perturbation assumed in the previous section is substituted into the Laplace equation (15). This allows the problem to be expressed as a general non-linear equation which can be solved iteratively.

Since the development of the non-linear equation is simple and straightforward, this solution method allows the theory [16] to be tested. If solving the inverse problem in this way proves to be successful, then solving the full analytical equation will be the next step. Solving with the exact equation will require integrating the Laplace transform [8, 10].

Assume the velocity perturbation is a series of step functions

$$v(u) = 4 \sum_{i=0}^{N} H(u_i; u) v_i, \tag{20}$$

where N is the number of steps and $H(u_i; u)$ are the step functions at each depth, u_i. Then Eq. (15) becomes

$$q^2F(q/2) = G(q) = 4\sum_{i=0}^{N} v_i \int_0^{\infty} du\, H(u_i;u) \exp(-qu_i) = 4\sum_{i=0}^{N} v_i\, q^{-1} \exp(-qu_i). \tag{21}$$

If $G(q)$ is discretized, then this equation can be solved iteratively; the non-linear inversion problem is

$$G(q_j) = 4\sum_{i=0}^{N} v_i q_j^{-1} \exp(-q_j u_i). \tag{22}$$

To solve a general non-linear equation of the form

$$\mathbf{f(m)} = \mathbf{d}, \tag{23}$$

where $\mathbf{m}$ are model parameters to be solved and $\mathbf{d}$ are the data, and given an initial estimate $\mathbf{m}_n^{est}$, a Taylor's expansion is made [14]

$$[\mathbf{f(m)} \approx \mathbf{f(m}_n^{est}) + \nabla\mathbf{f}[\mathbf{m} - \mathbf{m}_n^{est}] = \mathbf{f(m}_n^{est}) + F_n[\mathbf{m} - \mathbf{m}_n^{est}].$$

If $\Delta\mathbf{m}_{n+1} = [\mathbf{m} - \mathbf{m}_n^{est}]$, then

$$\mathbf{F}_n\Delta\mathbf{m}_{n+1} = \mathbf{d} - \mathbf{f(m}_n^{est}),$$

$$\mathbf{m}_{n+1}^{est} = \mathbf{m}_n^{est} + \Delta\mathbf{m}_{n+1}.$$

If the data are independent and have uniform variance then the least-squares solution is

$$\mathbf{m}_{n+1}^{est} = [\mathbf{F}_n^T\mathbf{F}_n]^{-1}\mathbf{F}_n^T[\mathbf{d} - \mathbf{f(m}_n^{est})] + \mathbf{m}_n^{est}.$$

For the current problem,

$$\mathbf{m} = (\mathbf{u}, \mathbf{v}),$$

$$\mathbf{d} = G(q_j) = (q_j^2F(q_j/2)) = 4\left(\frac{\alpha_1^2}{\alpha_2^2} - 1\right)\frac{\exp(-qh)}{q},$$

$$\mathbf{f} = (f_i(q_j)), f_i(q_j) = 4\sum_{i=0}^{N} v_i\, q_j^{-1} \exp(-q_j u_i),$$

$$\nabla\mathbf{f(m)} = \mathbf{F}, (F_{j,i}) = \frac{\partial f_j}{\partial m_i}.$$

For $\mathbf{u}$,

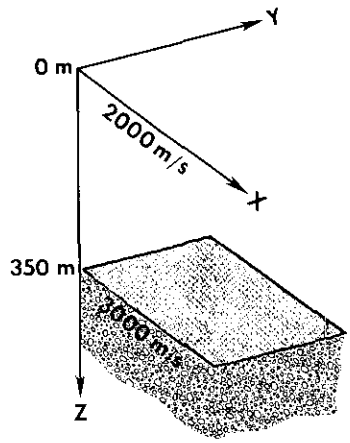

FIG. 1. Three-dimensional model used to generate the analytical and numerical datasets.

$$\frac{\partial f}{\partial u_i} = -4v_i \exp(-qu_i),$$

and for $\mathbf{v}$,

$$\frac{\partial f}{\partial v_i} = 4q^{-1} \exp(-qu_i).$$

A non-linear, least-squares method is a search for a best-fit solution under a particular norm. An easy way to visualize this search is to look at the error

$$\mathbf{e} = \mathbf{f(m)} - \mathbf{f(m}_n^{est}). \tag{24}$$

Assume that $\mathbf{m}$ is the solution to Eq. (24), then $\mathbf{e} = 0$ when $\mathbf{m}_n^{est} = \mathbf{m}$, the correct solution. Since $\mathbf{d}$ are exact for the analytical case above, $\mathbf{d} = \mathbf{f(m)}$ and

$$\mathbf{e} = \mathbf{f(m}_n^{est}) - \mathbf{d} = 0$$

when $\mathbf{m}^{est} = \mathbf{m}$. The error surface, $\mathbf{E}$, is defined as

$$\mathbf{E(m}_n^{est}) = |\mathbf{e(m}_n^{est})|.$$

Thus the position of a zero in the error surface $\mathbf{E}$ locates the correct model parameters, $\mathbf{m}$.

Let the input data be defined as Eq. (16) in the previous section. Substituting Eq. (16) into (21) and letting $N = 1$ gives

$$c_0^2(\alpha_2^{-2} - \alpha_1^{-2})\frac{\exp(-qh)}{q} = v\, q^{-1} \exp(-qu). \tag{25}$$

The error is zero when the parameters are exact (when $u = \mathbf{h}$ and $v = c_0(\alpha_2^{-2} - \alpha_1^{-2})$).

As an example, consider a single-layer over a half-space with velocities of 2000 m/s above and 3000 m/s below a reflector at a depth of 350 m (Fig. 1). Figure 2 presents several error-surface

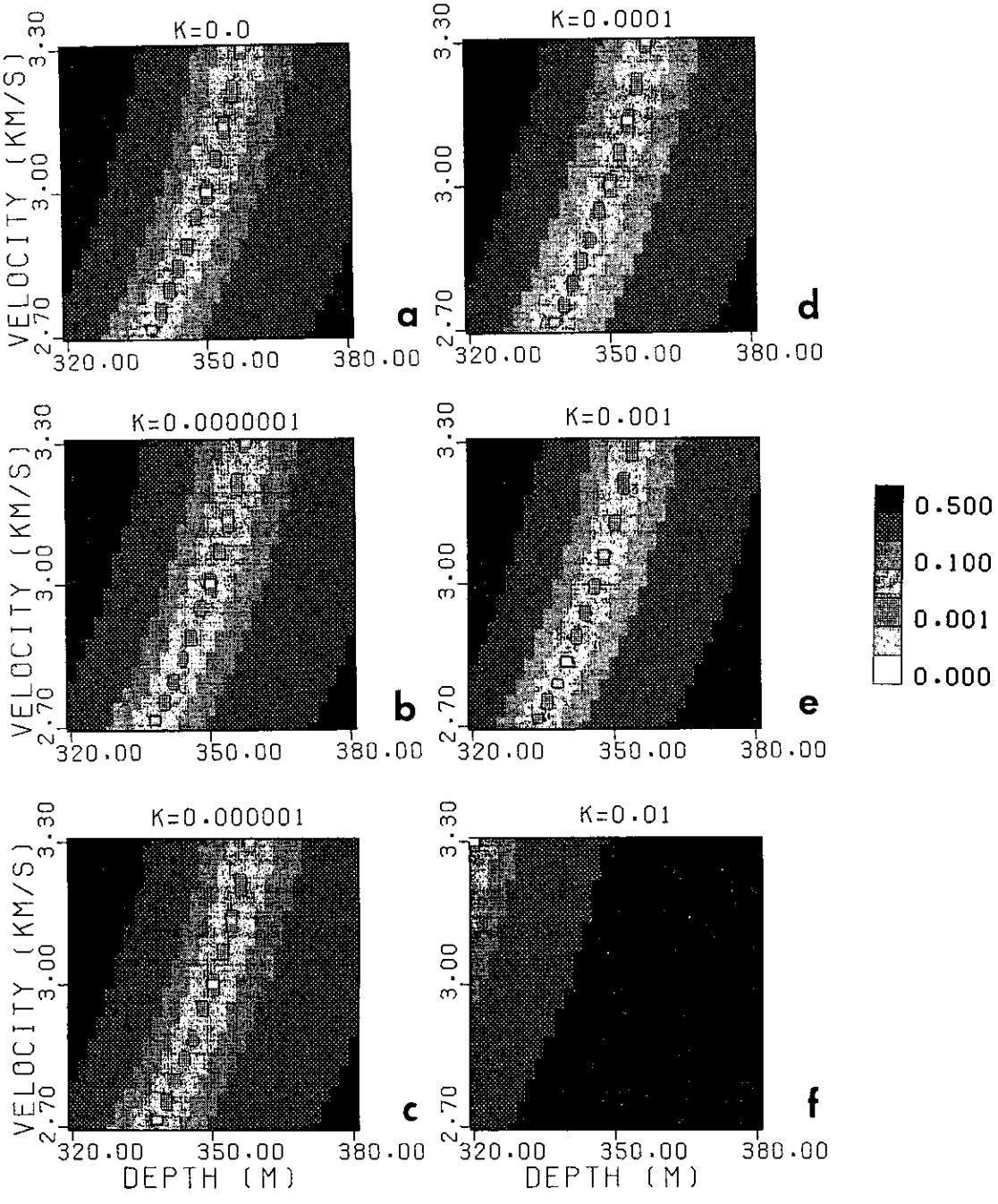

FIG. 2. Relative error surfaces (normalized to a maximum of 1.0) for the analytical dataset as a function of wavenumber, $k = \omega/v$. The correct solution is 350 m and 3000 m/s.

solutions to the corresponding non-linear, inverse problem with analytically defined data for various values of the background wavenumber $k = \omega/c_0$. In this figure and all similar ones following, the vertical axis is the velocity of the medium below the reflector calculated from the velocity perturbation [Eq. (19)]. The horizontal axis is the depth of the reflector, and gray scales give the amplitude of the error. The model parameters range $\pm 10\%$ from the true solution. An absolute minimum is located at the correct model parameter values as expected [Eq. (25)]; the minimum is found at the bottom of a trough extending from the top to the bottom of the error surface. Because the error surfaces are smooth, the non-linear inversion process will be stable.

Error surfaces for non-zero values of k were produced from

analytical data with the general analytical wave-equation solution without the zero frequency limit (Appendix B). They all have the same character as for $k = 0$ although, not surprisingly, the location of the central minimum moves away from the correct solution. These error surfaces are found over a range of low frequencies (Figs. 2b–2f) and show the same character as the zero-frequency case (Fig. 2a), but the minimum locations diverge from the correct ones for $k > 0.001$ radians/m. The absolute minimum error solutions are still found within an error of less than 10% up to $k = 0.001$ radians/m.

5. SYNTHETIC DATASET EXAMPLES

The evaluation of the solution [16] is continued in this section with a dataset generated by a 3D, scalar, finite-difference, forward-modeling program [3]. The first model is the same as that used in the analytic example above (Fig. 1). The 3D grid has 101 by 101 by 75 nodes with a grid spacing of 50 m. The impulsive source is located at the center of the grid ($X = 0$, $Y = 0$) at a depth of 50 m. The time section was generated for 800 time steps at 0.0025 s intervals for a total time of 2 s. The representative reflection section at $Y = 0$, $Z = 0$ is shown in Fig. 3a.

A second section was generated with a constant velocity model of 2000 m/s. This was subtracted from the reflective model to remove the direct wave (Fig. 3b). The periodic property of the discrete, 3D spatial Fourier transform to be applied allows the dataset to be reduced to one spatial quadrant since all four quadrants are symmetric. The remaining dataset was pseudo-deconvolved by replacing each trace with a spike of amplitude equal to the peak amplitude of the trace. The spike was located at the time of onset of the arrival of the reflected wavelet (Fig. 3c). The final step to prepare the data for input to the inversion was to perform a 3D Fourier transform of the $X \geq 0$ and $Y \geq 0$ quadrant for the 32 by 32 near-offset grid locations and 1024 zero-padded time samples.

The input to the non-linear problem consists of a subset of the 3D Fourier transform which can be viewed as a stack of planes, each of which corresponds to an increasing temporal frequency value. Each plane contains the offset wavenumber vector, $\mathbf{k}_h$. Appendix A shows that the independent variable q of Eq. (21) is closely related to the offset wavenumber; $q = |\mathbf{k}_h|$. A range of low-frequency planes were subjected to the inversion algorithm. Since the dataset is radially symmetric, the data along the line $\mathbf{k}_h = (k_x, k_y = 0)$ may be used as input data to avoid interpolation.

Error surfaces may be used to select the best solution, which is determined by the model parameters that minimize the error. Since there are only two parameters in this example (the interface depth and the lower-layer velocity) this solution method is simple and observable from inspection. However, it is necessary to solve for a third parameter, a source-amplitude-dependent scaling factor applied to the dataset, to make the data consistent with the analytical theory. Proper scaling requires

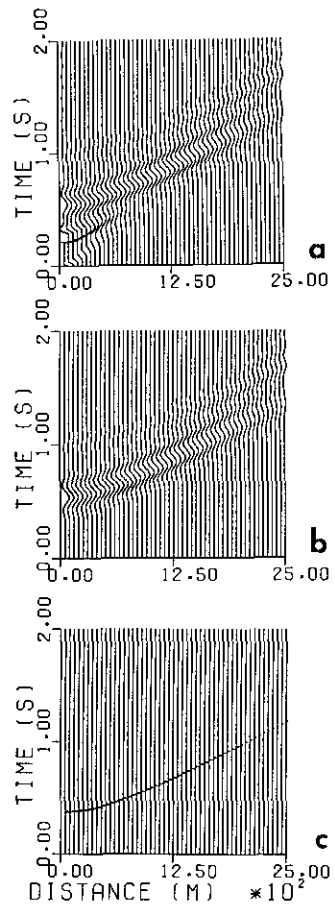

FIG. 3. Slices of seismograms along the X-axis from the center, generated from the model in Fig. 1: (a) total wavefield showing direct wave and reflection; (b) reflected wave only after subtracting the direct wave; (c) pseudo-deconvolved reflection.

analysis of the relation between the source time wavelet and the amplitude of its deconvolved amplitude (spike).

The scale factor was estimated in the following way. Let the solution be assumed known, *a priori*, to within ±10%. Since the velocity of the upper layer is also assumed to be known, the reflector depth can be estimated from the seismogram (see the Discussion). Then, the scale factor that minimizes the error over the entire velocity range of the estimated depth is used as the scale factor. The error to be minimized is the absolute error normalized by the scale factor (the relative error), since the absolute error is proportional to the scale factor.

Error surfaces for values of $k = \omega/c_0$ of zero and 0.0049135 are presented in Figs. 4a and 4b, respectively. Each of the surfaces has been independently normalized to a maximum value of one. In each figure, a prominent trough is superimposed on a sloping trend that increases from low velocity and shallow depths to higher velocities and deeper depths. As a result of the overall trend, the absolute minimum is located at the lower left end of the trough as shown in both figures. A locus of points defined as

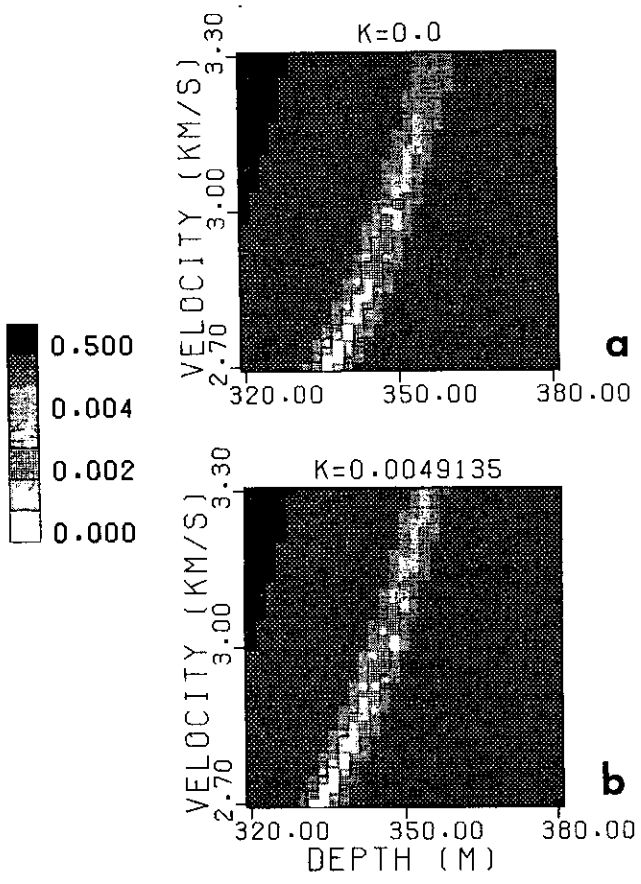

FIG. 4. Relative error surfaces (normalized to a maximum of 1.0) for the numerical dataset with a depth of 350 m for two wavenumbers.

the axis of the trough passes very close to the location for each pair of correct parameter values, and a local minimum is distinguishable within that locus in the vicinity of the same location.

Figure 5 shows the relative error for each of the three parameters (depth, velocity, scale factor) independently. For the depth parameter, the relative error shown in Fig. 5a is the minimum relative error across the entire surface as a function of velocity. The depth error graph illustrates the trough-like nature of the error surface. For the velocity parameter, the relative error shown in Fig. 5b is the minimum relative error across the entire surface as a function of depth. The velocity error graph illustrates the sloping trend of the trough locus and the difficulty of finding a local minimum on the error surface. The scale factor error in Fig. 5c was computed with the known, correct parameter values of velocity and depth.

Error surfaces for reflector depths of 250 and 450 m are shown in Fig. 6 for the lowest wavenumber values. These are similar to the previous case for a depth of 350 m (Fig. 4a) in that they have a trough tending upward from lower left to upper right, and they have local minima near the correct parameter values.

Error surfaces for all of the synthetic datasets show a striking similarity to the error surfaces generated from the analytical ones. The error trends from low to high parameter values are much steeper for the synthetic cases, but local minima are indicated near the correct parameter values. As in the analytic case, the error surfaces are smooth, so a non-linear, iterative process would be stable.

This numerical inversion was tested in the presence of noise. Several levels of random noise were added to the spiked (pseudo-deconvolved) dataset for a reflector depth of 350 m. The noise was distributed uniformly throughout the frequency spectrum. The noise level is defined as a percentage of the peak amplitude of the dataset. Figure 7a shows the noisy section and the corresponding error surface for 10% noise. Comparing to Fig. 4a, the surface appears smoothed by the noise addition. The trough is still present but only a hint of the local minimum remains. Similarly, Fig. 7b shows more of the same smoothing produced by the addition

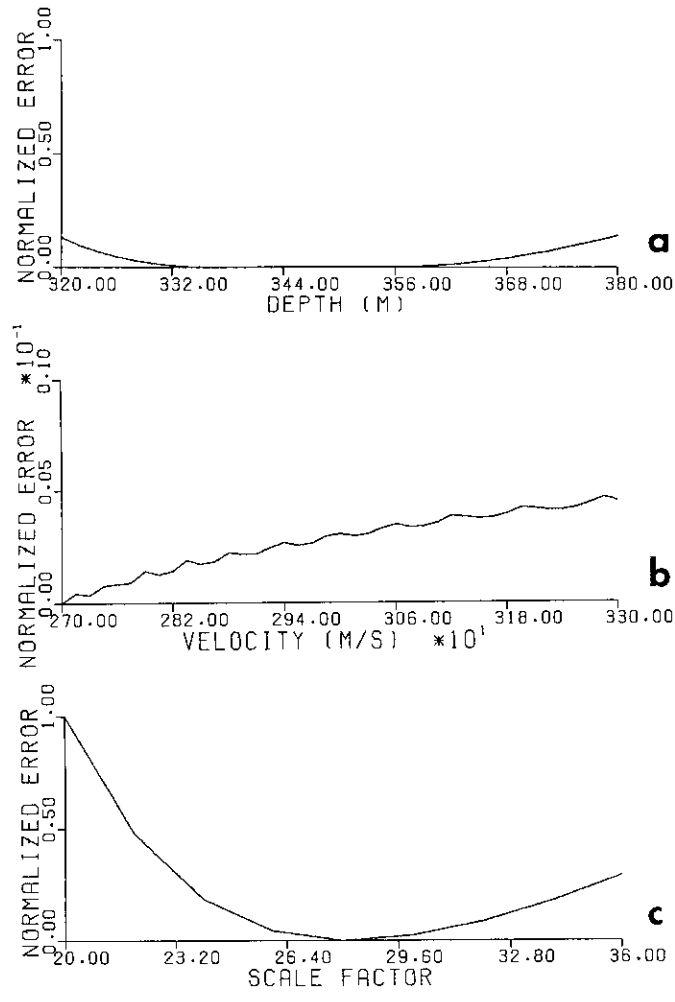

FIG. 5. Graphs of the error for the zero-wavenumber numerical dataset for a depth of 350 m (Fig. 4a): (a) along the depth axis; (b) along the velocity axis; (c) for values of the scale factor, with correct model parameters, normalized to one.

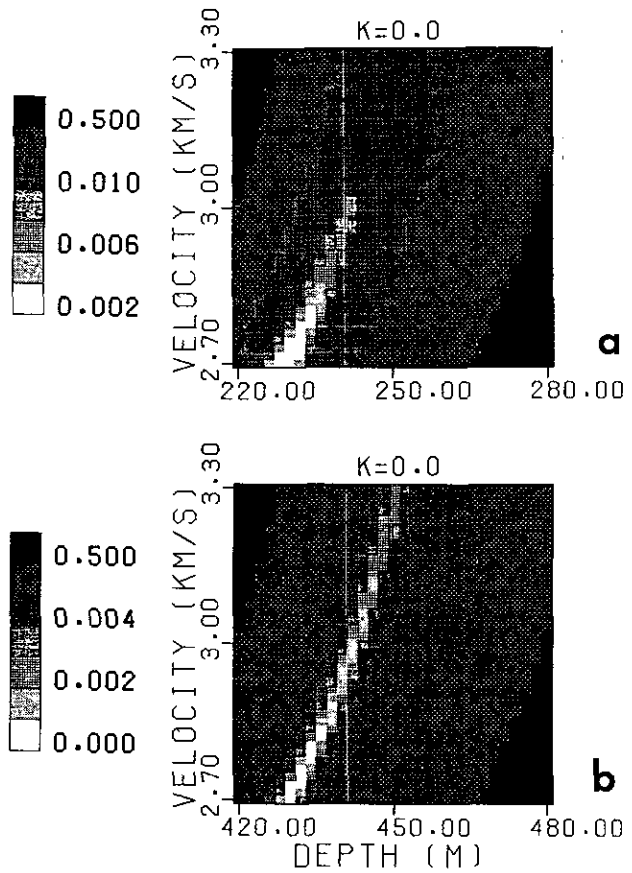

FIG. 6. Relative error surfaces (normalized to a maximum of 1.0) for numerical datasets where $k = 0$ for: (a) depth of 250 m; (b) depth of 450 m.

of 40% noise. Even for a noise level of 80% (Fig. 7c), the trough-like feature still appears.

6. DISCUSSION

During the computations of the inversion, it was observed that the position and character of the trough in the error surface were relatively insensitive to a bulk-time shift of the pseudo-deconvolved data. Thus, the reflector depth is constrained primarily by the hyperbolic shape of the reflection travel times, rather than by their absolute time position. This is consistent with the fact that the phase of the signal, which contains the absolute time information, is, by definition, zero at zero frequency. Consequently, adequate resolution of depth is contingent upon having sufficient spatial aperture in the observations.

Because the velocity of the upper layer is known, the depth of the reflector can be simply determined from the observed, normal-incidence, reflection travel time. This information can be reinserted into the inversion as a constraint; then by finding the intersection of the minimum error locus with the depth deduced from the reflection times, the solution for the velocity parameter can be determined. The reflection amplitudes are then the major determinants of the velocity of the lower layer. In this way, the inversion is complete, and both the depth and velocity can be accurately estimated.

Many of the low frequency datasets give similar error surfaces and nearly correct solutions. Choosing the best dataset and solution without any additional previous knowledge could be difficult. It is conceivable that weighted averages of the corresponding solutions could improve the resolution but, again, choosing the right datasets and weighting function could be difficult.

For the synthetic forward-modeling experiment, several sources of error can be identified such as the approximation of the scale factor. By simultaneously solving for all three parameters, an exact scale factor can be found that minimizes the error from scaling. Indeed, when a scale factor minimizing the error for the known depth and velocity parameters is estimated, better resolution of the experimental solution is achieved.

Another source of error comes from estimating reflection onset times. However, as mentioned above, the error surface is fairly independent of bulk-time shift errors.

This investigation of the potential of a low-frequency inversion algorithm [16] for the case of a single horizontal interface has demonstrated that it can be used to solve realistic seismic inversion problems. Although it works best in the zero frequency limit, it has been shown to work on finite frequencies extending into the potentially recordable range. It has also been shown to work for large velocity steps and in the presence of high-amplitude random noise.

With the one interface solution presented, multiple-layer models could be solved by a layer-stripping method, solving for each deeper layer after the parameters of the shallower ones are estimated. Alternately, the numerical inversion could be generalized to multiple horizontal surfaces simply by adding more parameters to the non-linear inverse system. For such a vastly expanded inversion, guaranteeing the convergence of the non-linear system would be much more difficult. However, by computing the inverse Laplace transform numerically, the velocity profile could be found directly.

This investigation has produced a potentially viable technique for solving for depth and velocity of the layers of an earth model. The inversion technique has been demonstrated for both analytically and numerically computed data. For potentially observable low frequencies, the error surface of the numerical dataset is quite similar to that computed analytically and has a solution very close to the correct parameters. Even in the presence of high-frequency random noise, solutions are obtainable.

Further investigation of this technique will include structures that are much deeper than the predominant wavelength, true deconvolution of the data and other waveform effects, sensitivity to background velocity, reflection beyond the

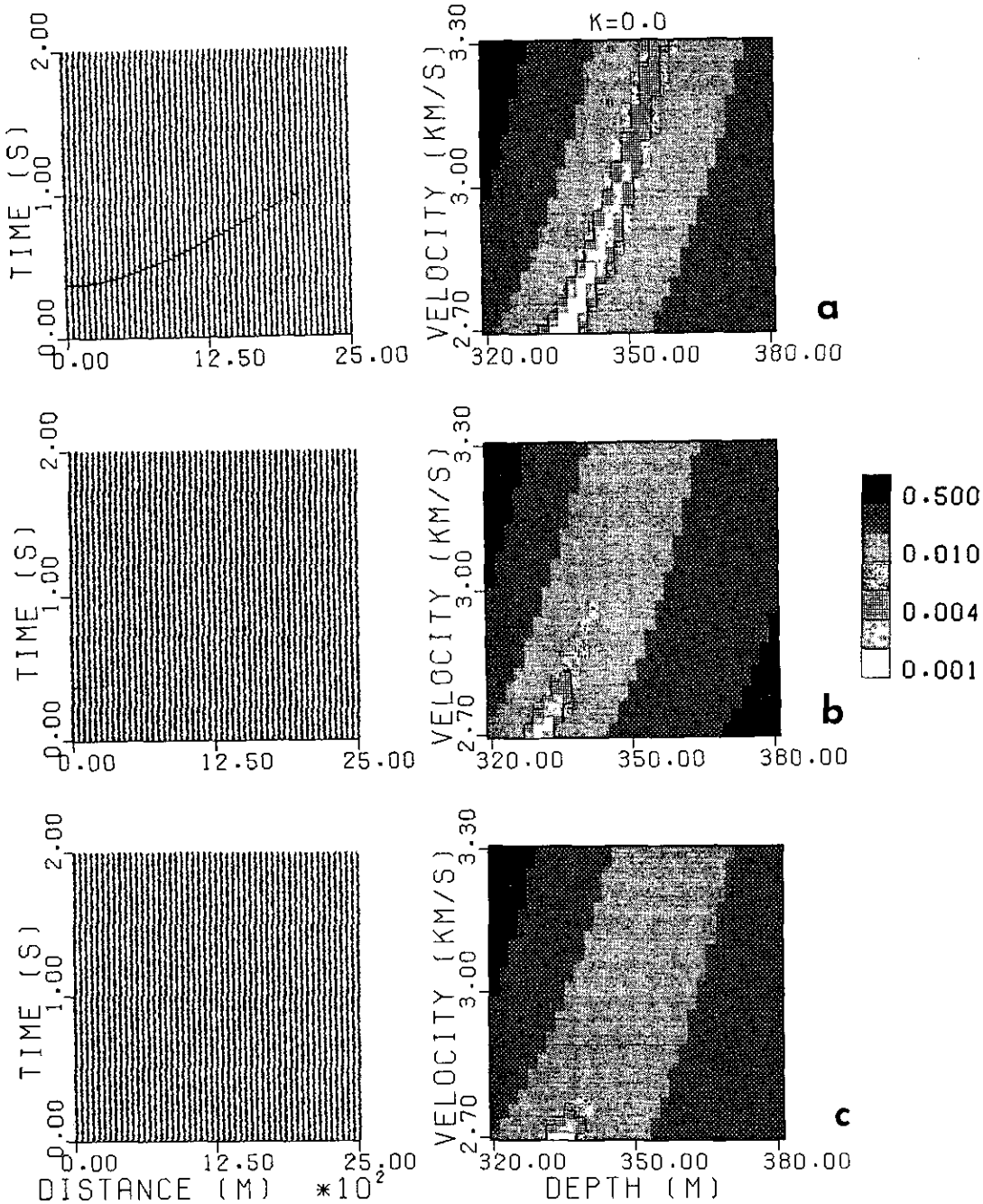

FIG. 7. Seismograms of the pseudo-deconvolved numerical zero-wavenumber datasets with random noise added along with the associated relative error surfaces for: (a) 10% noise level; (b) 40% noise level; and (c) 80% noise level. Seismogram amplitudes in (b) and (c) are scaled by 0.5 and 0.3, respectively, of those in (a).

critical angle, and the effects of low-frequency noise. Clearly, sufficiently large errors in the low-frequency part of the data will produce incorrect solutions. Effects of random low-frequency noise may be reduced by fitting over multiple independent observations, but this is one point that needs further investigation.

7. CONCLUSION

The theoretical importance of this solution [16] is that it is exact in the low-frequency limit; no approximations are needed for the solution. The goal of this research was to investigate the potential of this theoretical solution for solving practical problems. In theory, a complete velocity field for an arbitrary

subsurface structure could be found by performing the complete inversion of two inverse Fourier transforms and one inverse Laplace transform on the data. The only requirement is that the data contain sufficiently low frequency information and that this input be reliable.

The foregoing results encourage continuing effort toward the ultimate goal of inversion of actual field data. Since low-frequency data are required by this technique, earthquake or very-long-offset data may be especially well-suited for analysis by this method.

APPENDIX A

It has been shown in [16] that for a scalar wavefield $u = u(\mathbf{x}, \mathbf{y})$ with a source at $\mathbf{x} = (x_1, x_2, x_3)$ and receiver at $\mathbf{y} = (y_1, y_2, y_3)$, a medium with velocity $c(\mathbf{x})$ and a given reference or background velocity c_0 that

$$f(\mathbf{x}, \mathbf{y}) = 16\pi^2 \lim_{k\to 0} \left(\frac{u - g}{k^2}\right) = \int_{R_s} \mathbf{dz} \frac{v(\mathbf{z})}{|\mathbf{x} - \mathbf{z}|\,|\mathbf{z} - \mathbf{y}|}, \quad \text{(A1)}$$

where $\mathbf{z} = (z_1, z_2, z_3)$ is a spatial variable of integration, $v = c_0^2/c^2(\mathbf{x}) - 1$ is the perturbation velocity, and wavenumber $k = \omega/c_0$. The three-dimensional Green's function is

$$g(\mathbf{x}, \mathbf{y}) = \frac{\exp(ik\,|\mathbf{x} - \mathbf{y}|)}{4\pi\,|\mathbf{x} - \mathbf{y}|}. \quad \text{(A2)}$$

Note that $(u - g)$ is a measurable quantity, and thus f is computable and assumed to be given.

Equation (A1) can be solved [16] by Fourier transforming over $\mathbf{x}$ and $\mathbf{y}$ where $\mathbf{x} \} \boldsymbol{\lambda}$ and $\mathbf{y} \} \boldsymbol{\mu}$ are the corresponding transform variables. After a change of variables,

$$p_1 = \lambda_1 + \mu_1, \quad p_2 = \lambda_2 + \mu_2, \quad p_3 = |\boldsymbol{\lambda}|, \quad p_4 = |\boldsymbol{\mu}|,$$

the four-dimensional field is projected to a three-dimensional subfield using

$$q/2 = p_3 = p_4.$$

One implication of this projection is that the source wavenumber is required to be the same as the receiver wavenumber. This implies that the solution applies to waves that obey Snell's law.

The transformed equation (A1) is

$$\frac{q^2}{4} F(p_1, p_2, q/2, q/2) = \int_0^\infty du \exp(-qu) \frac{1}{4\pi^2} \int_{-\infty}^{+\infty} \int_{-\infty}^{+\infty} \mathbf{dz}' \exp[i(\mathbf{p}' \cdot \mathbf{z}'s)]\, v(\mathbf{z}', -u), \quad \text{(A3)}$$

where $\mathbf{p}' = (p_1, p_2)$ and $\mathbf{z}' = (z_1, z_2)$. The right-hand side of Eq. (A3), with cylindrical symmetry, contains the Fourier transform of the Dirac delta function, since $v(\mathbf{z}', -u)$ is independent of $\mathbf{z}'$. Thus

$$q^2 F(q/2) = 4 \int_0^\infty du \exp(-qu)\, v(-u) \quad \text{(A4)}$$

which gives Eq. (15) and is of a form similar to Eq. (13).

An interpretation of q is needed. The transform coordinates, (p_1, p_2, p_3, p_4), with the above restrictions, correspond to midpoint-offset domain wavenumbers, where the midpoint wavenumber is $\mathbf{k}_m = \mathbf{k}_s + \mathbf{k}_r$, the offset wavenumber is $\mathbf{k}_h = \mathbf{k}_s - \mathbf{k}_r$, $\mathbf{k}_s = \boldsymbol{\lambda}$ is the source wavenumber, and $\mathbf{k}_r = \boldsymbol{\mu}$ is the receiver wavenumber. Since $p_3 = p_4$, $|\boldsymbol{\lambda}| = |\boldsymbol{\mu}|$, $|\mathbf{k}_s| = |\mathbf{k}_r|$, and $|\mathbf{k}_h| = |\mathbf{k}_s - \mathbf{k}_r| = |\mathbf{k}_s| + |\mathbf{k}_s\mathbf{k}_r| + |\mathbf{k}_r| = 2\,|\mathbf{k}_r| = 2p_3$, then $q = |\mathbf{k}_h|$.

APPENDIX B

The analytic solution, ϕ, to the 3D, scalar wave equation, for the case of two half-spaces with velocities α_i and densities ρ_i for the ith layer and a source at height h above the lower half-space as given in Ewing *et al.* [9] is

$$\phi(r) = \phi_0 + \int_0^\infty d\kappa \left[\frac{\Delta\nu_1 - \nu_2}{\Delta\nu_1 + \nu_2}\right] \exp(-\nu_1(z + h)) \frac{\kappa J_0(\kappa r)}{\nu_1}, \quad \text{(B1)}$$

where $\nu_i = (\kappa^2 - \kappa_{\alpha_i}^2)^{1/2}$, $\kappa_{\alpha_i} = \omega/\alpha_i$, $\Delta = \rho_1/\rho_2 = 1$, and κ is the radial wavenumber. Constant density of the medium and equal depth for source and receivers are assumed. The direct wave (the free-space Green's function) is identified as ϕ_0. Then, following Eq. (A1),

$$\begin{aligned} f(r) &= 16\pi^2 \lim_{k\to 0} \left(\frac{\phi - \phi_0}{k^2}\right) \\ &= 16\pi^2 \lim_{k\to 0} \frac{1}{k^2} \int_0^\infty d\kappa \left[\frac{\nu_1 - \nu_2}{\nu_1 + \nu_2}\right] \frac{\exp(-2\nu_1 h)}{\nu_1} \kappa J_0(\kappa r). \end{aligned} \quad \text{(B2)}$$

If f is the Fourier transform of F (this convention is consistent with [16]), then

$$f(\mathbf{x}) = \int_{-\infty}^{+\infty} d\boldsymbol{\xi}\, F(\boldsymbol{\xi}) \exp(i\mathbf{x} \cdot \boldsymbol{\xi}) \quad \text{(B3)}$$

and

$$F(\boldsymbol{\xi}) = \frac{1}{4\pi^2} \int_{-\infty}^{+\infty} \mathbf{dx} f(\mathbf{x}) \exp(-i\,\boldsymbol{\xi} \cdot \mathbf{x}),$$

where $\boldsymbol{\xi} = (\xi_1, \xi_2)$, $\mathbf{x} = (x_1, x_2)$. Then, for $\rho = |\boldsymbol{\xi}|$, $r = |\mathbf{x}|$, and cylindrical symmetry, the relationship

$$f(r) = 4\pi^2 \int_0^\infty d\rho\, F(\rho)\, \rho\, J_0(\rho r) \quad \text{(B4)}$$

holds between the double Fourier transform and the Fourier–Bessel transform. Comparing Eq. (B2) and Eq. (B4), f and F are seen to be transform pairs where κ and ρ play the same roles; thus

$$F(\kappa) = 4 \lim_{k \to 0} \left(\frac{1}{k^2} \left[\frac{\nu_1 - \nu_2}{\nu_1 + \nu_2} \right] \frac{\exp(-2\nu_1 h)}{\nu_1} \right). \tag{B5}$$

Using L'Hopital's rule, the limit is found to be

$$F(\kappa) = c^2(\alpha_2^{-2} - \alpha_1^{-2}) \frac{\exp(-2\kappa h)}{2\kappa^3}. \tag{B6}$$

If F is a transform over $\mathbf{x}$ and $\mathbf{y}$, and f is radially symmetric with respect to $\mathbf{x}$

$$\begin{aligned} F(\boldsymbol{\lambda}, \boldsymbol{\mu}) &= \int_{-\infty}^{+\infty} \mathbf{dx} \int_{-\infty}^{+\infty} \mathbf{dy}\, f(\mathbf{x}, \mathbf{y}) \exp(-i\mathbf{x} \cdot \boldsymbol{\lambda}) \exp(-i\mathbf{y} \cdot \boldsymbol{\mu}) \\ &= \int_{-\infty}^{+\infty} \mathbf{dy}\, f(\mathbf{y}) \exp(-i\mathbf{y} \cdot \boldsymbol{\mu}), \quad \mathbf{x} = 0. \end{aligned} \tag{B7}$$

Then

$$f(\mathbf{y}) = \int_{-\infty}^{+\infty} \mathbf{d}\boldsymbol{\mu}\, F(\boldsymbol{\mu}) \exp(i\boldsymbol{\mu} \cdot \mathbf{y}). \tag{B8}$$

Substituting $\mathbf{x} = \mathbf{y}$ and $\boldsymbol{\mu} = \boldsymbol{\xi}$ into Eq. (B8) and comparing with Eq. (B4),

$$F(\rho) = F(|\boldsymbol{\mu}|). \tag{B9}$$

Since $|\boldsymbol{\mu}| = q/2 = \kappa$,

$$q^2 F(q/2) = 4c^2(\alpha_2^{-2} - \alpha_1^{-2}) \frac{\exp(-qh)}{q}, \tag{B10}$$

which is Eq. (16) in the text.

ACKNOWLEDGMENTS

The research leading to this paper was supported by Convex Computer Corporation (D.B.G.) and by the National Science Foundation under Grants EAR-9015852 and EAR-9204610 (G.A.M.). The authors gratefully acknowledge discussions with Dr. A. G. Ramm, and input and critical review by Dr. A. B. Weglein. *This paper is Contribution No. 795 from the Program in* Geosciences at the University of Texas at Dallas.

REFERENCES

1. M. Abramowitz and I. Stegun, *Handbook of Mathematical Functions* (U.S. Government Printing Office, Washington, DC., 1965), p. 1025.
2. N. Bleistein and J. K. Cohen, *Geophysics* **47,** 1497 (1982).
3. W. F. Chang and G. A. McMechan, *Geophys. Prosp.* **37,** 243 (1989).
4. J. F. Claerbout, *Geophysics* **36,** 467 (1971).
5. R. W. Clayton and G. A. McMechan, *Geophysics*, **46,** 860 (1981).
6. R. W. Clayton and R. H. Stolt, *Geophysics*, **46,** 1559 (1981).
7. J. Cohen and N. Bleistein, *Geophysics*, **44,** 1559 (1979).
8. B. Davies and B. Martin, *J. Comput. Phys.*, **33,** 1 (1979).
9. W. E. Ewing, W. S. Jardetsky, and F. Press, *Elastic Waves in Layered Media* (McGraw–Hill, New York, 1957), p. 93.
10. W. A. Essah and L. M. Delves, *Inverse Problems*, **4,** 705 (1988).
11. D. J. Foster and P. M. Carrion, *Geophysics*, **49,** 1794 (1984).
12. R. G. Keys and A. B. Weglein, *J. Math. Phys.* **24,** 1444 (1983).
13. P. A. Martin and A. B. Ramm, *Proc. R. Soc. London A* **399,** 153 (1985).
14. W. Menke, *Geophysical Data Analysis: Discrete Inverse Theory* (Academic Press, Orlando, Florida, 1984), p. 143.
15. P. Mora, *Geophysics*, **54,** 1575 (1989).
16. A. G. Ramm, *Phys. Lett. A* **99,** 258 (1983).
17. A. G. Ramm and A. B. Weglein, *J. Math. Phys.* **25,** 3231 (1983).
18. S. Raz, *Geophysics* **46,** 832 (1981).
19. R. H. Stolt and A. B. Weglein, *Geophysics* **50,** 2458 (1985).
20. A. Tarantola and B. Valette, *Rev. Geophys. Space Phys.* **20,** 219 (1982).
21. A. B. Weglein, *Geoexploration*, **20,** 47 (1982).
22. A. B. Weglein, in *Developments in Geophysical Methods 6,* edited by A. A. Fitch (Elsevier, London, 1985), p. 111.
23. A. B. Weglein and S. H. Gray, *Geophysics* **48,** 36 (1983).
24. A. B. Weglein, P. B. Violette, and T. H. Keho, *Geophysics* **51,** 1069 (1986).